



A coupled model of interior balanced and boundary flow



B. Deremble^a, E.R. Johnson^b, W.K. Dewar^{c,*}

^a LMD, Paris, France

^b Department of Mathematics, UCL, London, UK

^c Department of EOAS, FSU, Tallahassee, FL 32309, United States

ARTICLE INFO

Article history:

Received 22 May 2017

Revised 18 August 2017

Accepted 12 September 2017

Available online 14 September 2017

Keywords:

Mesoscale energetics

Quasi-geostrophic dynamics

Kelvin waves

ABSTRACT

Ocean circulation modeling requires parameterizations of sub-grid scale processes, which in turn involves two separate issues. First, the parameterization should mirror the effect of important sub-grid dynamics and second, constants and boundary conditions as required by the parameterization must be determined. In modern ocean circulation modeling, many parameterizations take the form of viscous operators with poorly known coefficients, and the boundary conditions options are free-slip, partial-slip or no-slip, suitably adjusted for the order of the operator. The extent to which viscous operators are dynamically apt is unclear and there is virtually no dynamical guidance on how to choose between the boundary conditions. Often the decision about the suitability of the parameterizations and the boundary conditions is made based on qualitative characteristics of the solution, which is somewhat subjective. Here, a dynamical boundary layer model is developed that explicitly determines the boundary potential vorticity fluxes resulting from the sub-grid scale interactions of the resolved flow with the boundaries. When applied to a quasi-geostrophic model, comparisons of model evolution with high resolution primitive equation simulations are favorable. The recipe outlined here, while far from a complete parameterization of boundary dynamics, represents a step toward resolving the issues currently surrounding sub-grid scale parameterization. The results also argue that boundary dynamics naturally dissipate balanced energy and are likely to represent a principal means by which the oceanic mesoscale energy budget is balanced.

Crown Copyright © 2017 Published by Elsevier Ltd. All rights reserved.

1. Introduction

Ocean circulation models employ sub-gridscale parameterizations often represented in the momentum equations as viscous-like operators where the order of the operator can be higher than second. While there are good numerical reasons for this choice, there is no real dynamical justification for it. Poorly known parameters are involved in them and, perhaps even more importantly, several different lateral boundary condition choices are available for them. It is a matter of well-known numerical experience that the nature of mature model circulation is quite sensitive to the sub-gridscale details, affecting such important features as Gulf Stream separation (Bryan et al., 2006; Schoonover et al., 2017). Indeed, the choices for parameter values and boundary conditions are often made based on which combination results in qualitative model features, such as Gulf Stream separation, that are most realistic. Guidance in sub-gridscale parameterization from dynamical considerations would be of great value, but this is an area in which progress has been slow. The purpose of this paper

is to contribute to this topic through examination of a category of boundary mechanics that results in a viscous-like control on interior flows. In contrast to existing parameterizations, the results are relatively insensitive to details of the implementation. We suggest that the approach taken here is a step toward a more complete dynamically based prescription for interior-boundary interactions. A second result is that boundary dynamics are likely to be a significant sink of interior mesoscale energy.

1.1. Background

The problem of parameterization and boundary condition choices in ocean circulation models arose with the earliest dynamical circulation models. Stommel (1948) avoided lateral boundary conditions by the use of a bottom drag; Munk (1950) with a frictional operator used no-slip boundary conditions. In both cases, the parameterizations and boundary conditions were central to the solutions so obtained. The first attempts at numerical circulation modeling were based in quasi-geostrophic (qg) dynamics and a variety of viscous operators and boundary condition combinations were attempted. A clear demonstration of the solution dependence on the choice of either partial slip or no-slip appears in

* Corresponding author.

E-mail addresses: wdewar@fsu.edu, dewar@ocean.fsu.edu (W.K. Dewar).

[Haidvogel et al. \(1992\)](#). While the no-flux boundary condition is appropriate for the flow normal to the boundary, the physically suggested no-slip boundary condition on the tangential flow is less clear due to model discretization ([Adcroft and Marshall, 1998](#)). The manner in which the free-slip/no-slip choice affects the interior in realistic models with irregular coastlines is also an issue ([Adcroft and Marshall, 1998](#)).

Most modern ocean simulations are based on the primitive equations which, while dynamically richer than qg, still exhibit a strong dependence on boundary interactions. [Bryan et al. \(2006\)](#) systematically investigated parameterization and resolution sensitivities of a North Atlantic circulation model and illustrated the dependency of Gulf Stream separation to them. Here the type of boundary condition was held fixed (they employed free-slip), however the values and grid-scalings of the viscous coefficients result in vastly different behaviors. The effects, being centered on Gulf Stream separation, demonstrate the importance of both the explicit boundary condition and the amplitude of the various parameters.

Most modern circulation models employ a combination of second (Laplacian) and higher order sub-grid scale parameterizations with parameter values tuned to provide a circulation close to that of the real ocean (see [Chassignet and Garraffo, 2001](#) and [Madec, 2006](#)). While the results are often quite pleasing according to this metric, it is recognized that there is a real need for a better dynamical understanding of boundary physics in order to remove some of this ambiguity.

The model developed in this paper is offered as a step in this direction. The analysis is strongly rooted in qg dynamics, in which the most significant shortcoming of the boundaries relative to the real ocean is the restriction to vertical walls. However, the physics that arise involve interior flow interaction with boundary waves and, as such, clear dynamical analogs exist with wave types belonging to more complicated topography and sloping boundaries. In addition, favorable comparisons with primitive equation results suggest that the involved dynamics transcend qg parameteric limitations. We propose that qg has in this case illuminated processes relevant to the primitive equations, as it has done frequently in other past settings, such as eddy dynamics. In the present setting, it is connections between small scale boundary dynamics and the interior balanced flow that have been captured in the dynamical boundary layer model (DBM) appended to the interior equations. This study builds on [Dewar et al. \(2011\)](#) where the boundary dynamics were explored in isolation from their feedback onto the interior. The present study seeks to close the problem by properly coupling the DBM and the interior so that they evolve simultaneously.

While some degree of success has been achieved in this exercise, the parameterization is by no means complete. Rather, one aspect, hopefully a significant one, of boundary dynamics is extracted from the complete physical system and clarified.

Model development is given in [Section 2](#), and is followed by comparisons between a suite of models in the next section. Impacts on the system energetics are investigated in [Section 4](#) and the paper ends with a summary and discussion of future work.

2. Model development

We start with the hydrostatic equations written in density coordinates

$$\frac{\partial}{\partial t} u + u \frac{\partial}{\partial x} u + v \frac{\partial}{\partial y} u + H \frac{\partial}{\partial \rho} u - fv = - \frac{\partial}{\partial x} M + X \quad (1a)$$

$$\frac{\partial}{\partial t} v + u \frac{\partial}{\partial x} v + v \frac{\partial}{\partial y} v + H \frac{\partial}{\partial \rho} v + fu = - \frac{\partial}{\partial y} M + Y \quad (1b)$$

$$\frac{\partial}{\partial \rho} M = gz \quad (1c)$$

$$\frac{\partial}{\partial t} \frac{\partial}{\partial \rho} z + \nabla \cdot \left(\mathbf{u} \frac{\partial}{\partial \rho} z \right) + \frac{\partial}{\partial \rho} e = 0 \quad (1d)$$

where u, v are horizontal velocities, f the Coriolis frequency, ρ density, z depth of a density surface, (X, Y) 'viscous' effects and M the Montgomery potential,

$$M = p + (\rho - \rho_0)gz \quad (2)$$

with p dynamic pressure and ρ_0 a reference density. The quantity H represents the non-conservative processes affecting density, i.e.

$$\frac{d}{dt} \rho = H \quad (3)$$

and is related to the entrainment, e , by

$$e = H \frac{\partial}{\partial \rho} z \quad (4)$$

The depth variable, z , is broken into a background part dependent only on ρ and a fluctuation

$$z = \bar{z}(\rho) + z'(x, y, \rho, t) \quad (5)$$

In keeping the usual quasi-geostrophic (qg) approach, \bar{z} (analogous to N^2 in a level model) is assumed known. The equations are now scaled in the classical qg way. The result is

$$\epsilon \left(\frac{\partial}{\partial t} u + u \frac{\partial}{\partial x} u + v \frac{\partial}{\partial y} u + \Lambda H \frac{\partial}{\partial \rho} u \right) - fv = - \frac{\partial}{\partial x} M + X_o X \quad (6a)$$

$$\epsilon \left(\frac{\partial}{\partial t} v + u \frac{\partial}{\partial x} v + v \frac{\partial}{\partial y} v + \Lambda H \frac{\partial}{\partial \rho} v \right) + fu = - \frac{\partial}{\partial y} M + Y_o Y \quad (6b)$$

$$\frac{\partial}{\partial \rho} M = z \quad (6c)$$

$$\left(\frac{\partial}{\partial \rho} \bar{z} \right) \nabla \cdot \mathbf{u} + \epsilon \left(\frac{\partial}{\partial t} \frac{\partial}{\partial \rho} z + \nabla \cdot \left(\mathbf{u} \frac{\partial}{\partial \rho} z \right) \right) + \Lambda \frac{\partial}{\partial \rho} e = 0 \quad (6d)$$

where f and all other variables are now non-dimensional and the prime has been dropped from the perturbation depth. The parameter $\epsilon = U_0/(fL)$ is the Rossby number. The scalings for the frictional and diapycnal terms are X_o, Y_o and Λ , respectively and are assumed small.

Following well-known methods, the above are expanded in powers of the Rossby number, leading eventually to the qg equation written in density coordinates

$$\frac{\partial}{\partial t} q + \frac{1}{f} J(M_o, q) = - \nabla \cdot \mathbf{F}_q; \quad q = \frac{1}{f} \nabla^2 M_o - \frac{f}{z_\rho} \frac{\partial^2}{\partial \rho^2} M_o \quad (7)$$

where M_o is the lowest order contribution to the Montgomery potential, which is analogous to the more familiar equation in depth coordinates. Here \mathbf{F}_q is the flux of pv due to non-conservative effects and other notation is standard. The explicit form of \mathbf{F}_q is

$$\mathbf{F}_q = \left(\frac{\Lambda}{\epsilon} H \frac{\partial}{\partial \rho} v_o - \frac{Y_o}{\epsilon} Y \right) \mathbf{i} + \left(\frac{X_o}{\epsilon} X - \frac{\Lambda}{\epsilon} H \frac{\partial}{\partial \rho} u_o \right) \mathbf{j} \quad (8)$$

and is consistent with the results of [Marshall et al. \(2001\)](#). We will assume (7) holds everywhere in the basin interior. Having shown how non-conservative effects (i.e. e and X, Y) appear in qg, we will not include them for convenience in the following analysis. They will eventually be included again where needed.

We examine the possibility that the essential dynamics on the boundary are richer than simple qg. In particular, we are interested in interactions between the interior qg flow and flows

on the boundary, where Kelvin waves (Pedlosky, 2013) are active. Low mode Kelvin waves when viewed from a qg perspective are too fast to be perturbed at leading order by the circulation, but higher mode Kelvin waves move more slowly and can be expected to interact with the qg flows. Such modes are also associated with short spatial scales in the horizontal (high mode deformation radii) and vertical (high mode number). We will build a boundary layer model for qg by introducing these two short spatial scales in a standard multiple scales analysis.

The procedure will be illustrated for the western boundary layer, although generalization to other boundaries is straightforward. We simply substitute

$$\frac{\partial}{\partial x} \rightarrow \frac{\partial}{\partial x} + \frac{1}{\epsilon} \frac{\partial}{\partial \chi} \quad (9a)$$

$$\frac{\partial}{\partial \rho} \rightarrow \frac{\partial}{\partial \rho} + \frac{1}{\epsilon} \frac{\partial}{\partial \Gamma} \quad (9b)$$

where χ is a short zonal variable of $O(\epsilon)$ relative to the first baroclinic deformation radius and Γ is a short density interval of $O(\epsilon)$ relative to the full density range, for the existing zonal and density derivatives in (6a). All variables are now expanded in powers of the Rossby number ϵ .

2.1. Multiscale expansion

The leading order equations are somewhat different than the usual qg result due to the presence of the fast variables

$$\frac{\partial}{\partial \chi} \left(u_o \frac{\partial}{\partial \Gamma} z_o \right) + \frac{\partial}{\partial \rho} \bar{z} \frac{\partial}{\partial \chi} u_o = 0 \quad (10a)$$

$$\frac{\partial}{\partial \chi} M_o = \frac{\partial}{\partial \Gamma} M_o = 0 \quad (10b)$$

$$u_o \left(\frac{\partial}{\partial \chi} v_o + f \right) = - \frac{\partial}{\partial y} M_o \quad (10c)$$

Eq. (10a) can be written

$$\frac{\partial}{\partial \chi} \left(u_o \frac{\partial}{\partial \Gamma} z_o + \left(\frac{\partial}{\partial \rho} \bar{z} \right) u_o \right) = 0 \quad (11)$$

as the mean state stratification \bar{z} depends only on ρ . Thus, because the quantity $u_o (\frac{\partial}{\partial \Gamma} z_o + \frac{\partial}{\partial \rho} \bar{z})$ is a constant throughout the boundary layer, the no-flux condition at the boundary requires it to be zero. We also assume the stratification is non-trivial, so in the boundary layer

$$u_o = 0 \quad (12)$$

which is expected in qg theory. This however does not imply $\frac{\partial}{\partial x} u_o$ vanishes in the boundary layer. A second ramification of (12) is

$$\frac{\partial}{\partial y} M_o = 0 \quad (13)$$

(see 10c) or that leading order pressure on the boundary is a constant. Again, this agrees with classical qg analysis.

At the next order in Rossby number, one obtains

$$\begin{aligned} \frac{\partial}{\partial t} \frac{\partial}{\partial \Gamma} z_o + \left(\frac{\partial}{\partial \Gamma} z_o + \frac{\partial}{\partial \rho} \bar{z} \right) \left(\frac{\partial}{\partial x} u_o + \frac{\partial}{\partial y} v_o + \frac{\partial}{\partial \chi} u_1 \right) \\ + u_1 \frac{\partial}{\partial \Gamma} \frac{\partial}{\partial \chi} z_o + v_o \frac{\partial}{\partial \Gamma} \frac{\partial}{\partial y} z_o = 0 \end{aligned} \quad (14a)$$

$$\frac{\partial}{\partial \rho} M_o + \frac{\partial}{\partial \Gamma} M_1 = z_o \quad (14b)$$

$$f v_o = \frac{\partial}{\partial x} M_o + \frac{\partial}{\partial \chi} M_1 \quad (14c)$$

$$\frac{\partial}{\partial t} v_o + u_o \frac{\partial}{\partial x} v_o + v_o \frac{\partial}{\partial y} v_o + u_1 \frac{\partial}{\partial \chi} v_o + u_o \frac{\partial}{\partial \chi} v_1 + f u_1 = - \frac{\partial}{\partial y} M_1 \quad (14d)$$

where u_o has been retained for the moment. Eqs. (10c) and (14c) can be used to eliminate M_o

$$f \left(\frac{\partial}{\partial x} u_o + \frac{\partial}{\partial y} v_o \right) = - \frac{\partial}{\partial x} u_o \frac{\partial}{\partial \chi} v_o + \frac{\partial}{\partial y} \frac{\partial}{\partial \chi} M_1 \quad (15)$$

Note that the form of (15) converges to leading order divergence-free flow as $\chi \rightarrow \infty$.

Similarly, (14d) and (10c) can be used to eliminate M_1

$$\begin{aligned} \frac{\partial}{\partial t} \frac{\partial}{\partial \chi} v_o + u_1 \frac{\partial^2}{\partial \chi^2} v_o + v_o \frac{\partial}{\partial \chi} \frac{\partial}{\partial y} v_o \\ + \left(\frac{\partial}{\partial \chi} v_o + f \right) \left(\frac{\partial}{\partial x} u_o + \frac{\partial}{\partial y} v_o + \frac{\partial}{\partial \chi} u_1 \right) = 0 \end{aligned} \quad (16)$$

Eq. (16) can be combined with (14a) to yield

$$\frac{D}{Dt} \left(\frac{\frac{\partial}{\partial \chi} v_o + f}{\frac{\partial}{\partial \Gamma} z_o + \frac{\partial}{\partial \rho} \bar{z}} \right) = 0 \quad (17)$$

where

$$\frac{D}{Dt} = \frac{\partial}{\partial t} + u_1 \frac{\partial}{\partial \chi} + v_o \frac{\partial}{\partial y} \quad (18)$$

Eq. (17) is the potential vorticity equation of the boundary layer and reduces to the identity

$$\frac{D}{Dt} \frac{f}{\frac{\partial}{\partial \rho} \bar{z}} = 0; \quad \chi \rightarrow \infty \quad (19)$$

Eq. (17) is analogous to the pv equation used in Dewar et al. (2011) and describes dynamics on the small boundary scales. We segregate the boundary dynamics from the interior dynamics by requiring the boundary responses to have vanishing pv anomaly,

$$\frac{\frac{\partial}{\partial \chi} v_o + f}{\frac{\partial}{\partial \Gamma} z_o + \frac{\partial}{\partial \rho} \bar{z}} = \frac{f}{\frac{\partial}{\partial \rho} \bar{z}} \quad (20)$$

Using (10b) and (14c) reduces (20) to

$$\frac{\partial^2}{\partial \chi^2} M_1 - \frac{f}{\frac{\partial}{\partial \rho} \bar{z}} \frac{\partial^2}{\partial \Gamma^2} M_1 = 0 \quad (21)$$

which is the elliptic equation also appearing in Dewar and Hogg (2010) and Dewar et al. (2011). The solution of this equation is obtained by projecting it on the complete set of orthogonal functions defined by the eigenvalue problem

$$\frac{\partial^2}{\partial \Gamma^2} F_n - \frac{\frac{\partial}{\partial \rho} \bar{z}}{f} \lambda_n^2 F_n = 0; \quad \frac{\partial}{\partial \Gamma} F_n = 0; \quad \rho = (\rho_s, \rho_b) \quad (22)$$

The equation resulting from (21) admits growing and decaying exponentials, the latter of which is retained to be consistent with the boundary layer analysis (see Dewar and Hogg, 2010 for a discussion of the linear limit).

2.2. Boundary-interior connection

At this point, the analysis has shown the interior pv equation is faced with a constant pressure on the boundary, but the value of the constant is unknown. In addition, the dynamics of the

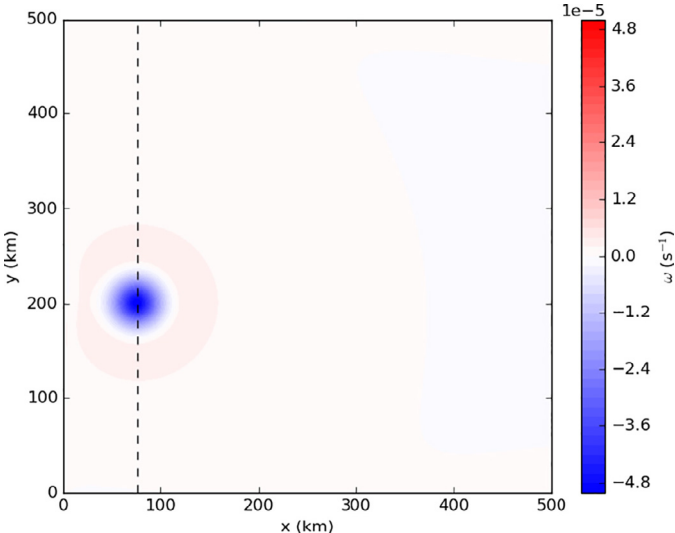


Fig. 1. Surface vorticity profile (same initial condition used in all three models).

boundary layer reside in the elliptic Eq. (21) that needs boundary conditions at $\chi = 0$ for a unique solution.

The first step to obtain this information is to evaluate (14d) at the wall

$$\frac{\partial}{\partial t} v_o + v_o \frac{\partial}{\partial y} v_o + \frac{\partial}{\partial y} M_1 = 0 \quad (23)$$

Integrating (23) around the domain yields

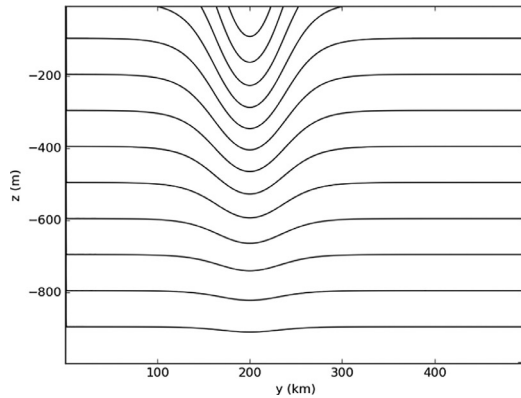
$$\frac{\partial}{\partial t} \int_{\partial A} \mathbf{v}_o \cdot \mathbf{n} dl = 0 \quad (24)$$

provided the along wall velocity is continuous. If, as in the classical qg equations, the along wall flow is provided only by the interior geostrophic dynamics, (24) becomes

$$\frac{\partial}{\partial t} \int_{\partial A} \nabla M_o \cdot \mathbf{n} dl = 0 \quad (25)$$

which is the usual condition determining the boundary Montgomery potential value (see McWilliams, 1977).

However, in the present case, from (14c), the quantity v_o is seen to consist of two parts, a geostrophic part connected to the interior and a geostrophic (in the along wall direction) part that belongs to the boundary. Thus, (23) can be rewritten



$$\begin{aligned} \frac{\partial}{\partial t} \frac{\partial}{\partial \chi} M_1 + v_g \frac{\partial}{\partial y} \frac{\partial}{\partial \chi} M_1 + \frac{\partial}{\partial \chi} M_1 \frac{\partial}{\partial y} v_g \\ + \frac{\partial}{\partial \chi} \frac{M_1}{f} \frac{\partial}{\partial y} \frac{\partial}{\partial \chi} M_1 + f \frac{\partial}{\partial y} M_1 = -f \left(\frac{\partial}{\partial t} v_g + v_g \frac{\partial}{\partial y} v_g \right) \end{aligned} \quad (26)$$

where v_g denotes the interior geostrophic meridional velocity evaluated at $x = 0$.

Note that the solution of (26) is a prediction for the normal derivative of M_1 and, as such, is the boundary condition needed to uniquely solve (21). Eq. (26) is also the equation solved in Dewar et al. (2011) to compute the forced Kelvin wave response given a specified interior geostrophic field. The differences here are that the interior is allowed to evolve dynamically and interact with the boundary response via the solution to (23). The boundary connection to the interior remains to be determined.

Eq. (26) is hyperbolic and the characteristic solution of it leads to isopycnals pinching together, and the unphysical result that v_o becomes multivalued (see Dewar et al., 2011). At such locations, we instead require that fronts form and stabilize when the isopycnals become vertical (i.e. they are so-called 'weak' or discontinuous solutions (Whitham, 1974) of (23). The fully developed forms for the fronts are characterized by

$$\frac{\partial}{\partial \chi} v_o + f = \frac{\partial}{\partial \Gamma} z_o + \frac{\partial}{\partial \rho} \bar{z} = 0 \quad (27)$$

The latter constraint is equivalent to the layer thickness vanishing, while the former is a statement of zero absolute vorticity and is needed for the potential vorticity to remain finite. With vanishing layer thickness, and associated discontinuities in along-wall velocity, the quantity v_o becomes

$$v_o = v_s + \sum_i \Delta v_i H(\mathbf{x} - \mathbf{x}_i) \quad (28)$$

where v_s is a smooth function, \mathbf{x} is a location on the boundary and the index i denotes the front at location \mathbf{x}_i . The function H is related to the usual Heaviside function and is defined by

$$H(x) = 0; \quad x < 0; \quad H(0) = 1/2; \quad H(x) = 1; \quad x > 0 \quad (29)$$

In other words, the along wall velocity is a smooth function interrupted by a series of step discontinuities. The various derivatives in (26) thus involve Dirac delta functions, and the full line integral in (25) becomes a sum of measures of the discontinuities at the fronts. Recalling that the full along wall velocity is composed of both a (smooth) interior geostrophic velocity and a wall response

$$\frac{\partial}{\partial t} \int_{\partial A} \mathbf{v}_g \cdot \mathbf{n} dl = -\sum_i \left(\left(-\frac{\partial}{\partial t} \mathbf{x}_i \right) \Delta(v_i) + \Delta \frac{v_i^2}{2} + \Delta M_{1,i} \right) \quad (30)$$

where $\frac{\partial}{\partial t} \mathbf{x}_i$ denotes the rate at which the front at \mathbf{x}_i moves. According to (30), fronts modify net geostrophic circulation which, in turn, influences the value of the boundary Montgomery potential.

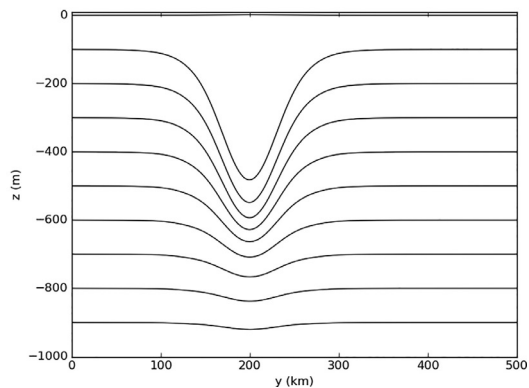


Fig. 2. Left: vertical temperature profile along the dashed line in Fig. 1 for the MITgcm (contour interval: 0.5 K). Right: position of the isopycnals in GOLD along the same section.

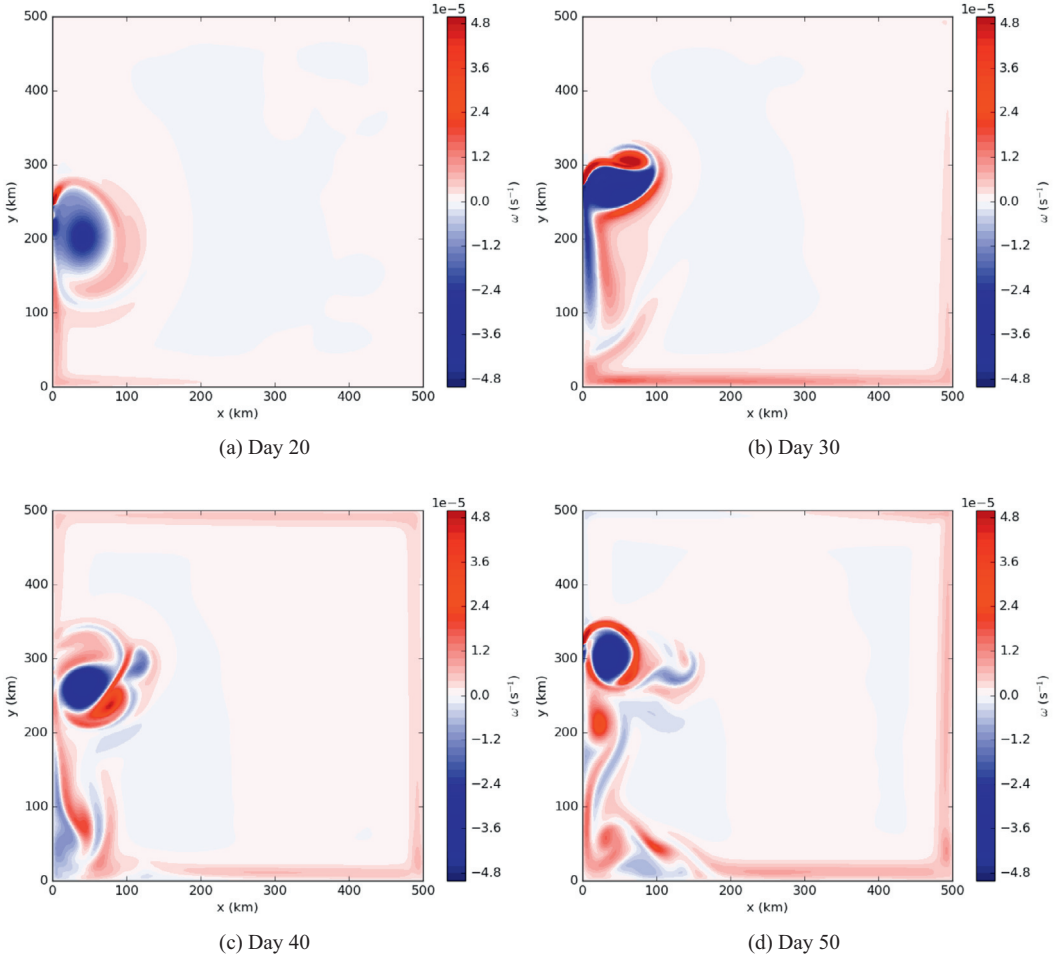


Fig. 3. Snapshots of the surface relative vorticity at days 20, 30, 40 and 50 (moving clockwise from the upper left) from GOLD.

A change in net circulation is equivalent to a change in integrated vorticity, which implies the appearance of new vorticity in the interior, so it is still necessary to indicate how the circulation changes in (30) appear as qg vorticity. Recalling that in the presence of viscous effects, the adiabatic (i.e. $e = 0$) qg equation is

$$\frac{d}{dt}q_o = -\nabla \cdot \mathbf{F}_q = \frac{\partial}{\partial x}Y - \frac{\partial}{\partial y}X \quad (31)$$

where viscous scalings have been set to unity and X, Y are the nonconservative effects working on the momentum equations. When solving the viscous qg equations numerically, it is thus necessary to apply a net boundary pv flux to the equations, which for a north-south boundary consists of the value of Y on the boundary.

The full boundary velocity equation including viscous effects is

$$\frac{\partial}{\partial t}v_o + v_o \frac{\partial}{\partial y}v_o + \frac{\partial}{\partial y}M_1 = Y \quad (32)$$

where Y is expected to be small everywhere but in the fronts. With Y explicitly present, the structure for v_o becomes smooth (i.e. the fronts are no longer discontinuous, but are locations of very large but finite gradients), so if we consider an integration over a boundary segment from just behind a front to just ahead of a front, there results

$$\left(-\frac{\partial}{\partial t}y_i\right)\Delta v_i + \Delta\left(\frac{v_i^2}{2}\right) + \Delta M_{1,i} = \int_{y_i^-}^{y_i^+} Y dy \quad (33)$$

Equivalently, the value of the net boundary flux at the frontal location is determined by the front parameters. Effectively, the

front injects vorticity into the domain, where the ultimate source of the vorticity is viscosity. The full solution of the qg system thus consists of simultaneously solving the qg equation (with (30) as a boundary condition) and (32), using the latter to determine the pv flux from the boundaries into the interior via (33). The Eqs. (30), (32) and (33) constitute our DBM.

3. Numerical examples

We have implemented the above procedure in the quasi-geostrophic model Q-GCM (Hogg et al., 2003). The viscous term Y is parameterized as an along wall Laplacian acting on v_o , which with the viscous coefficient used here ($\nu = 50 m^2/s$) was sufficient to control the fronts.

We have compared the parameterized qg evolution with numerical solutions obtained using the MITgcm (Marshall et al., 1997) and the isopycnal model GOLD (Hallberg, 2000) run at high resolution.

Parameters typical of a mid-latitude β plane ocean have been used, i.e. $f = 10^{-4} s^{-1}$ and $\beta = 2 \times 10^{-11} s^{-1}$. The basic state stratification for the MITgcm was set by a linear temperature profile in the vertical

$$T_b = \Delta T \left(1 - \frac{z}{H}\right), \quad (34)$$

with $H = 1000$ m the depth of the water column and $\Delta T = 5$ K the temperature difference between the top and the bottom. The same profile was used to determine layer temperatures in both

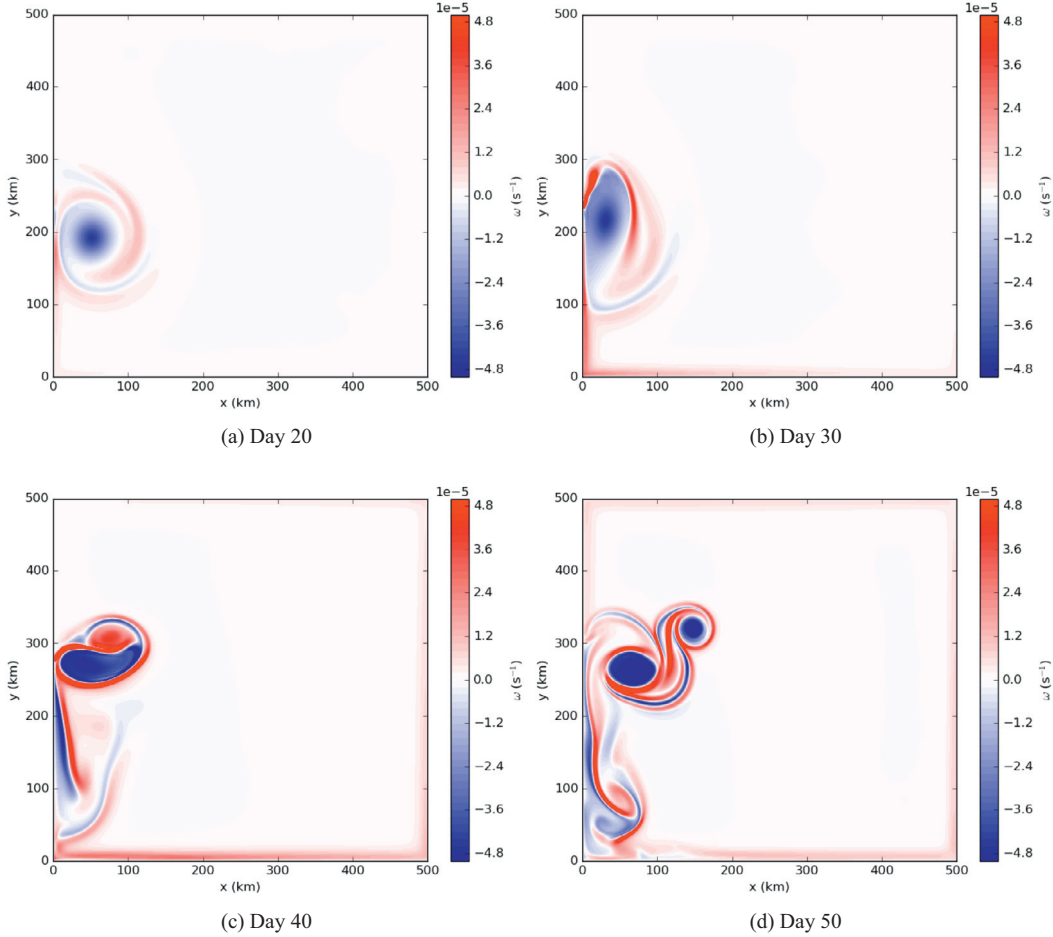


Fig. 4. Snapshots of the surface relative vorticity at days 20, 30, 40 and 50 for the MITgcm.

GOLD and Q-GCM. A linear equation of state is used with thermal expansion coefficient $\alpha = 2 \times 10^{-4} \text{ K}^{-1}$.

We consider the initial value problem of a monopolar vortex situated 75 km east and 200 km north of the southwestern corner of a $500 \text{ km} \times 500 \text{ km}$ domain (see Fig. 1). The form used for the vortex was

$$\nu_\theta(r) = \nu_0 F(z) \frac{\tanh(r/r_0)}{\cosh^2(r/r_0)}, \quad (35)$$

with

$$F(z) = 1 - erf(z/z_0) \quad (36)$$

where r is a radial coordinate extending from vortex center, $r_0 = 75 \text{ km}$, $z_0 = 500 \text{ m}$ and ν_θ is the corresponding swirl velocity. The initial vortex position was sufficiently far from the boundaries that the above formulas were used without modification at the walls.

The horizontal structure of the vortex is a continuous approximation of the Rankine vortex (Doswell, 1984). At any height z , we use the geostrophic balance to recover the pressure field

$$\frac{dp}{dr} = f\nu_\theta, \quad (37)$$

which can in turn be used to infer the density field via the hydrostatic balance. The vertical function (36) is chosen such that both the velocity and the density anomalies are maximum at the surface. This field is used to initialize the three models, all of which employ a 1 km horizontal resolution. The MITgcm employs 100 levels with a resolution of 10 m, while GOLD and Q-GCM both use 10 layers with a constant reduced gravity of 10^{-3} ms^{-2} . The

vertical profile of temperature from the MITgcm and the layer thicknesses from GOLD are plotted in Fig. 2. Note that there is no outcropping in the layered model because all of the outcropped densities in the MITgcm are contained within in the uppermost GOLD model layer. We use a harmonic viscosity of $\nu = 50 \text{ m}^2 \text{ s}^{-1}$ for GOLD and Q-GCM, $\nu = 10 \text{ m}^2 \text{ s}^{-1}$ for MITgcm and free slip boundary conditions in all cases.

3.1. Results

A typical vortex sequence as shown in surface relative vorticity appears in Fig. 3 from the GOLD experiment, in Fig. 4 for the MITgcm experiment and in Fig. 5 from the Q-GCM experiment. Early on the vortex migrates westward toward the wall due to β . As it is squeezed on the wall it deforms and propagates northward as expected from 'image' (see Crosby et al. (2013) and references therein) dynamics (Day 20). This part of the evolution is entirely consistent with purely balanced dynamics. For unknown reasons, the initial westward vortex drift differs between the models; the GOLD vortex arrives at the wall a few days earlier than in either the MITgcm or Q-GCM (compare Figs. 4 and 5).

Upon commencing northward propagation, a very strong cyclonic vorticity filament is peeled away from the wall by the vortex in all models (Figs. 3a, b; 4 a, b; 5 a, b). The source of the vorticity is, however, not a frictional sublayer as the boundary conditions are free slip. This part of the evolution has no analog in inviscid qg theory. A similar result was seen in Dewar and Hogg (2010), and the explanation provided there involved the

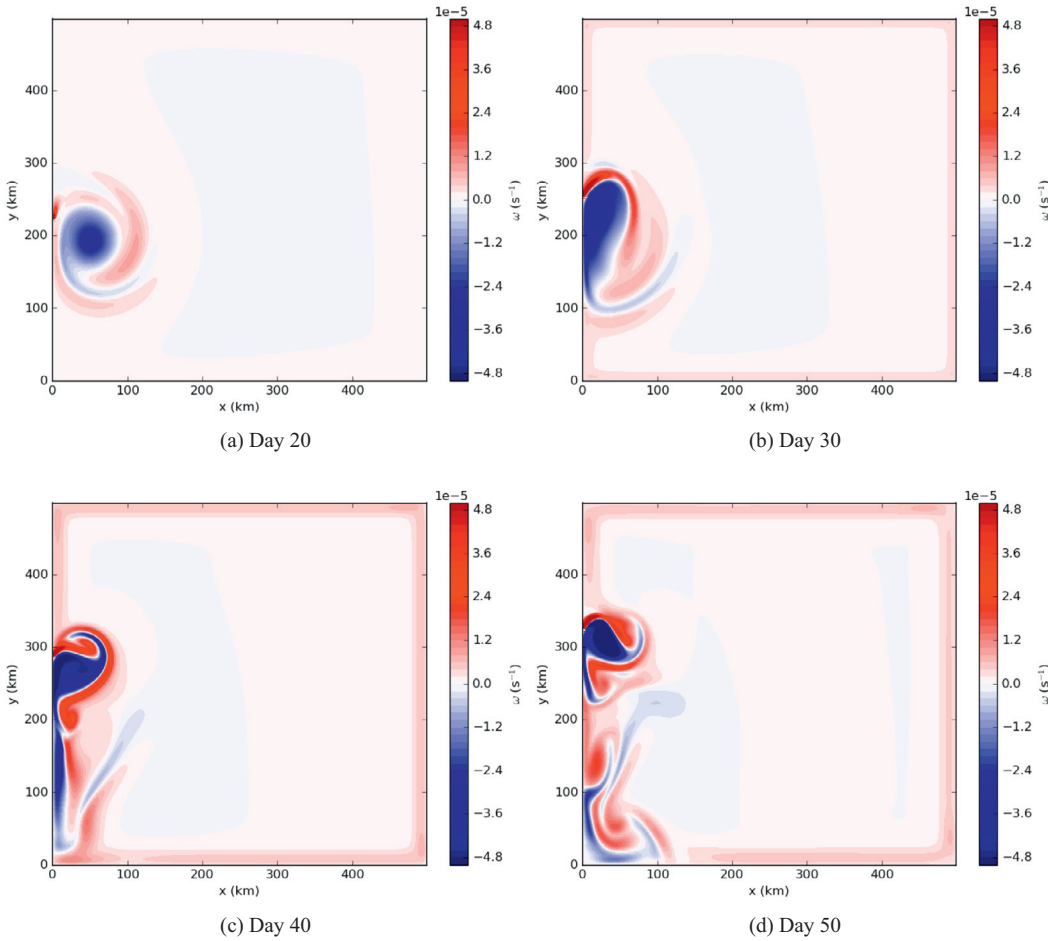


Fig. 5. Snapshots of the surface relative vorticity at days 20, 30, 40 and 50 for the Q-GCM.

arresting of southward propagating Kelvin waves by the northward directed flows of the anticyclonic vortex.

If sufficiently strong, the newly formed cyclonic filament rolls up onto itself to form a macroscopic cyclone (Fig. 3b) which pairs up with the primary anticyclone to form a dipole. This occurs for all three models, although the strength of the cyclonic partner varies and so the subsequent evolution can follow more than one path. The asymmetric pair in GOLD moves the primary vortex away from the wall and they follow a curved trajectory eventually returning to the wall ((see Days 30 and 40); Fig. 3b and c). The GOLD dipole splits when it again encounters the wall: the cyclone moves southward and the anticyclone resumes its northward migration. At this point, a new cycle of cyclonic vorticity generation begins (Fig. 3d).

The details of the dipolar evolution are highly dependent on the amount of newly created vorticity at the boundary. Strong vorticity creation (compared to the vorticity of the primary vortex), moves the pair faster away from the wall and, as seen in the MITgcm results, can even split the primary vortex into two parts (cf. Fig. 4d). For weak vorticity generation, the positive vorticity filament may simply be advected around the primary cyclone without forming a coherent vortex. In such a situation, the primary vortex may not move away from the wall. This is seen early in the Q-GCM vortex, although continued cyclonic vorticity generation eventually results in a cyclonic vortex.

Figs. 6–8 illustrate the vorticity injection process. Here, the interface displacement (contours) and velocity (colors) on the wall are plotted. In all three cases, as the anticyclone migrates northward, the upper layers 'pinch' such that the flow in these layers

is blocked. Most importantly, there is effectively a discontinuity in the velocity profile and the Montgomery potential in these layers upon which we base the PV injection in the qg model (see (33)). This is consistent with the mean flow-Kelvin wave interaction idea that the anticyclone presence is critical to maintaining the discontinuity. Indeed, if the subsequent evolution moves the vortex away from the boundary, the front can dissolve. This is seen at Day 40 in Fig. 6c, where the vortex has been forced away from the wall by the newly created cyclone. As the cycle restarts, we observe strong similarities between the plots in Fig. 6b and d. The sequences displayed in these figures are not identical, but agree qualitatively in the marked evolution of the wall isopycnals and the appearance of cyclonic vorticity.

The initial condition in these experiments consists only of anticyclonic vorticity and, for that matter, negative pv anomaly (not shown). Cyclonic vorticity for the most part appears in areas consistent with our explanation based on front formation, i.e. it streams from regions on the wall slightly north of the vortex center. However, cyclonic vorticity also appears elsewhere in many of the plots, as in Fig. 3b–d. The other cyclonic zones are not of a wall origin, as can be seen in Fig. 9a, which shows potential vorticity at Day 40 from the GOLD results. Note in particular the cyclonic streamer along the southwestern boundary between 50 km and 200 km in Fig. 3c. This feature is visible in pv as a streamer whose value is not anomalously high; rather at $pv \times 10^{-6} m^{-1} s^{-1}$ it corresponds to the background. Since the wall injects pv into the system and the cyclonic streamer is not anomalous in pv, it is clear that cyclonic vorticity is a result of conservative pv evolution. In contrast, the large region of intense cyclonic vorticity paired

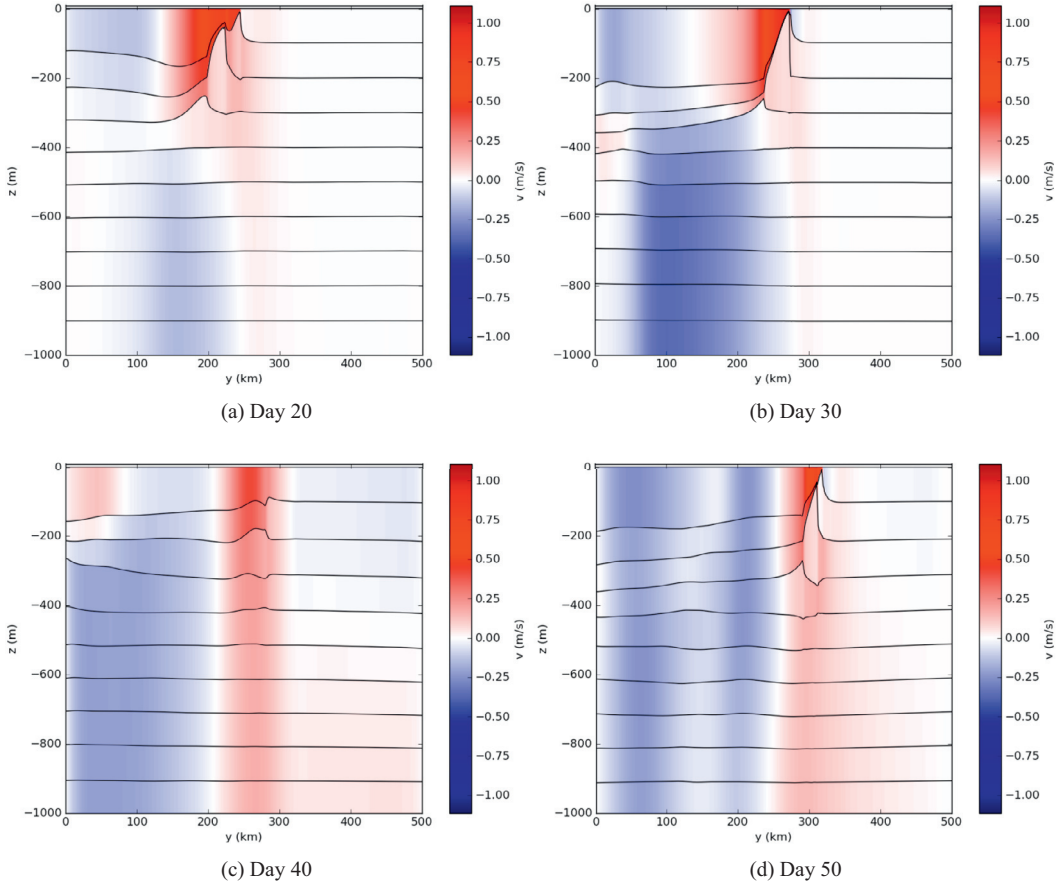


Fig. 6. Snapshots of the along wall velocity (color) and interface displacement (contours) days 20, 30, 40 and 50 for GOLD.

with the original vortex in Fig. 3c corresponds to a strong positive pv anomaly in Fig. 9a. Because such pv is not present in the initial condition, it can only be the result of wall injection. Such behavior is characteristic of the pv fields in both the GOLD and MITgcm runs. An example of pv from the Q-GCM at Day 40 appears in Fig. 9b. Here again a positive pv anomaly appears at the location of cyclonic vorticity, but nowhere else. By construction, the source of this pv is due to the wall interaction, which supports our theoretical modeling.

In Fig. 10, we plot the time series of the mean circulation in the upper layer (total circulation divided by the area of the domain). Recall that the models all employ free-slip boundaries, so the boundary effect on circulation would normally be expected to be small. This is what happens initially. Until day 20 there is no significant variation in the circulation as the vortex moves westward toward the wall. However, between day 20 and day 40 strong circulation changes are seen, even to the point of reversing the sign of the circulation. At day 40, the mean circulation is about 10 times stronger than its initial absolute value. This increase corresponds to the injection of cyclonic filaments into the domain (see Figs. 3–5). As mentioned previously, the injection starts earlier in GOLD. After the initial injection, we expect the three curves to only qualitatively match: in MITgcm, the injection is stronger and forces the vortex further away from the wall such that the next peel off and strong circulation change do not occur before day 70.

In Fig. 10, we also add a curve for an MITgcm experiment using $\nu = 50 \text{ m}^2 \text{ s}^{-1}$ (dashed red line) instead of $\nu = 10 \text{ m}^2 \text{ s}^{-1}$ as discussed previously. For this configuration (using the same viscosity as GOLD and Q-GCM), the vorticity injection was much weaker and inadequate for the formation of a coherent cyclone. The reason for this distinction is due to the potentially very different physical

effects of 'horizontal' viscosity in isopycnal and level models. Away from fronts where isopycnals have small slopes, layer horizontal and level horizontal viscosity play comparable roles. Near fronts, however, 'horizontal' layer viscosity in transferring momentum along isopycnals acts almost in a vertical sense, whereas in a level model, momentum transfers are largely across isopycnals. This works to smooth the along wall velocity profile for a level model such that front formation and the accompanying vorticity injection are suppressed. The tendency for the isopycnals to form fronts in that experiment was largely suppressed (not shown).

4. Energetics consequences

Consider now the balanced energetics of a closed basin. This is obtained by multiplying the qg pv equation by the Montgomery potential and integrating by parts.

$$\begin{aligned}
& \int_{\rho_s}^{\rho_b} \int_S \left(M_o \frac{\partial}{\partial t} q + M_o \mathbf{u}_o \cdot \nabla q \right) \frac{\partial}{\partial \rho} \bar{z} dA d\rho \\
&= \int_V \left(M_o \frac{\partial}{\partial t} q_o + M_o \mathbf{u}_o \cdot \nabla q_o \right) dV \\
&= -\frac{\partial}{\partial t} \int_V \left[\frac{(\nabla M_o)^2}{2f} - \frac{f}{\frac{\partial}{\partial \rho} \bar{z}} \frac{(\frac{\partial}{\partial \rho} M_o)^2}{2} \right] dV \\
&\quad + \int_z \left[\oint M_o \frac{\partial}{\partial t} \nabla M_o \cdot \mathbf{n} dl \right] dz - \int_S f_o w_e M_o dA \\
&= - \int_V M_o \nabla \cdot \mathbf{F}_Q dV
\end{aligned} \tag{38}$$

where w_e denotes any Ekman pumping energy source. The no-normal flow conditions have been used to eliminate advection and

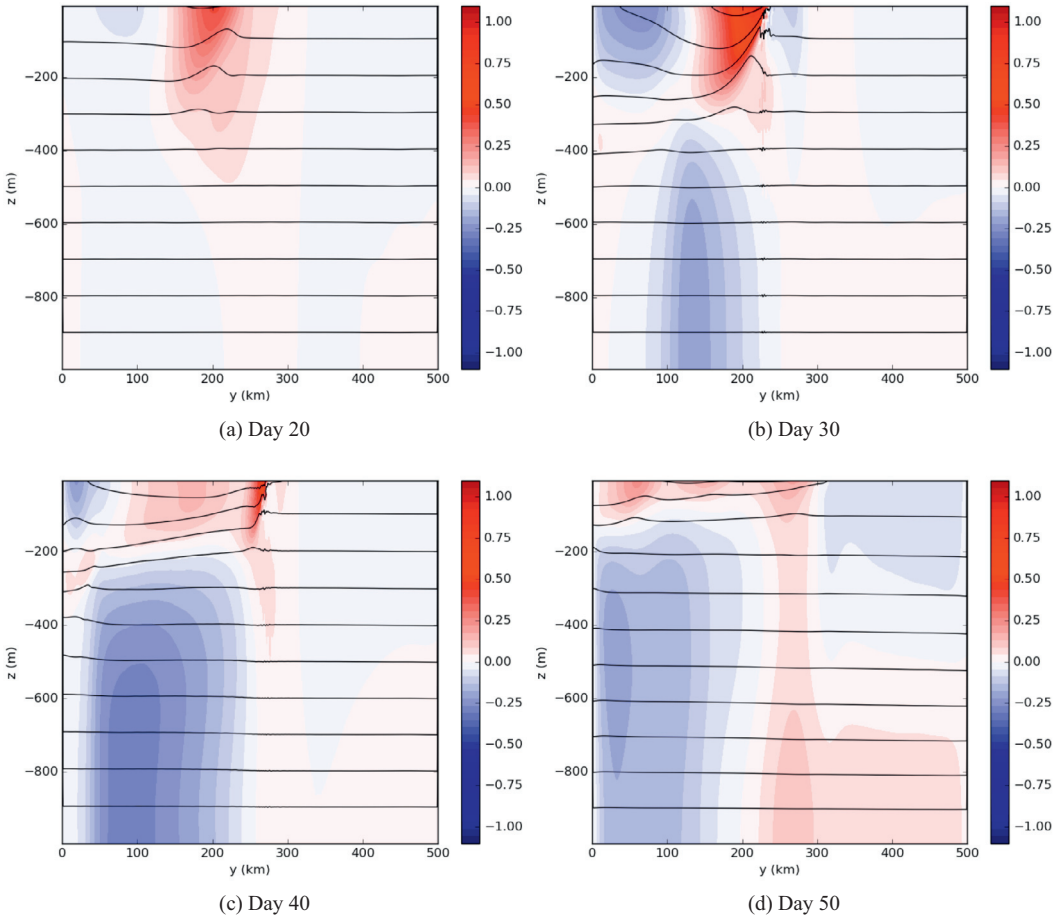


Fig. 7. Snapshots of the along wall velocity (color) and temperature (contours; contour interval = 0.5 K) days 20, 30, 40 and 50 for the MITgcm.

the domain extends into the overlap region of the boundary layer where q_g is still accurate. The boundary layer analysis assures that the leading order Montgomery on the edge must be a constant on any isopycnal, thus allowing it to be migrated outside of the boundary line integral in (38). The result is

$$\frac{\partial}{\partial t} \int_V (K + P) dV = - \int_S w_e M_0 dA + \int_z M_0 \int \frac{\partial}{\partial t} \nabla \frac{M_0}{f} \cdot \mathbf{n} dl dz - \Xi \quad (39)$$

where free slip boundaries have been used,

$$K = \frac{(\nabla M_0)^2}{2f} \quad (40)$$

and

$$P = \frac{f}{\frac{\partial}{\partial \rho} \bar{z}} \frac{(\frac{\partial}{\partial \rho} M_0)^2}{2} \quad (41)$$

are the kinetic and potential energies seen in (38) and Ξ denotes viscous loss proportional to velocity gradients squared integrated over the domain.

A statement about the net geostrophic circulation change is needed to complete the equation. This is obtained from (30), such that (39) becomes

$$\frac{\partial}{\partial t} \int_V (K + P) dV = - \int_S w_e M_0 dA - \Xi - \int_z \sum_i \left(\left(\left(-\frac{\partial}{\partial t} \mathbf{x}_i \right) \Delta (\nu_o) + \Delta \frac{v_o^2}{2} - \Delta M_1 \right) M_0 \right) dz \quad (42)$$

Thus the fronts governed by (26) act like an energy sink on the interior balanced flow. Physically the sink represents flow up the

pressure gradients along the boundaries set up and maintained by the wall dynamics.

Eq. (42) (with $w_e = 0$) can be used to examine the energetics in the present case. Fig. 11 (left) compares the time evolution of the kinetic and potential energy relative to their initial values in the three models. The curves all show their strongest behavior from days 20 to 40 during the period of strong wall-vortex interaction. Consistently among the three models, potential energy transfers aggressively to kinetic energy during this interval. The level of kinetic energy reached after 40 days is about twice its initial value (not shown). After 40 days, the APE dropped by 50% in both Q-GCM and Gold and 25% in MITgcm (not shown). After 40 days in MITgcm, we mentioned previously that the interaction with the wall is less pronounced as the eddy moves away from the wall. This tendency is also visible in the PE and KE curves. Note also the overall energetic behavior differs between the MITgcm and the layer models. This is due to the differences in model construction and the differing trajectories of the vortex relative to the wall.

Total energy evolutions from the three model runs appear in Fig. 11 (right). Very early (< 20 day) energy decreases slowly at a rate that can be accounted for from internal dissipation, Ξ . This changes significantly once the vortices begin interaction with the boundary. Consistent with our earlier discussion, total energy decays first for GOLD, where the vortex experiences its earliest encounter with the wall. Both GOLD and Q-GCM exhibit roughly comparable decay rates. The MITgcm is considerably slower in energy loss. However, upon inspection of Fig. 7, it is seen that after the initial wall encounter, the cyclone is able to push the vortex away from the boundary much more effectively in the MITgcm than in the other models. As a result, the MITgcm cyclonic

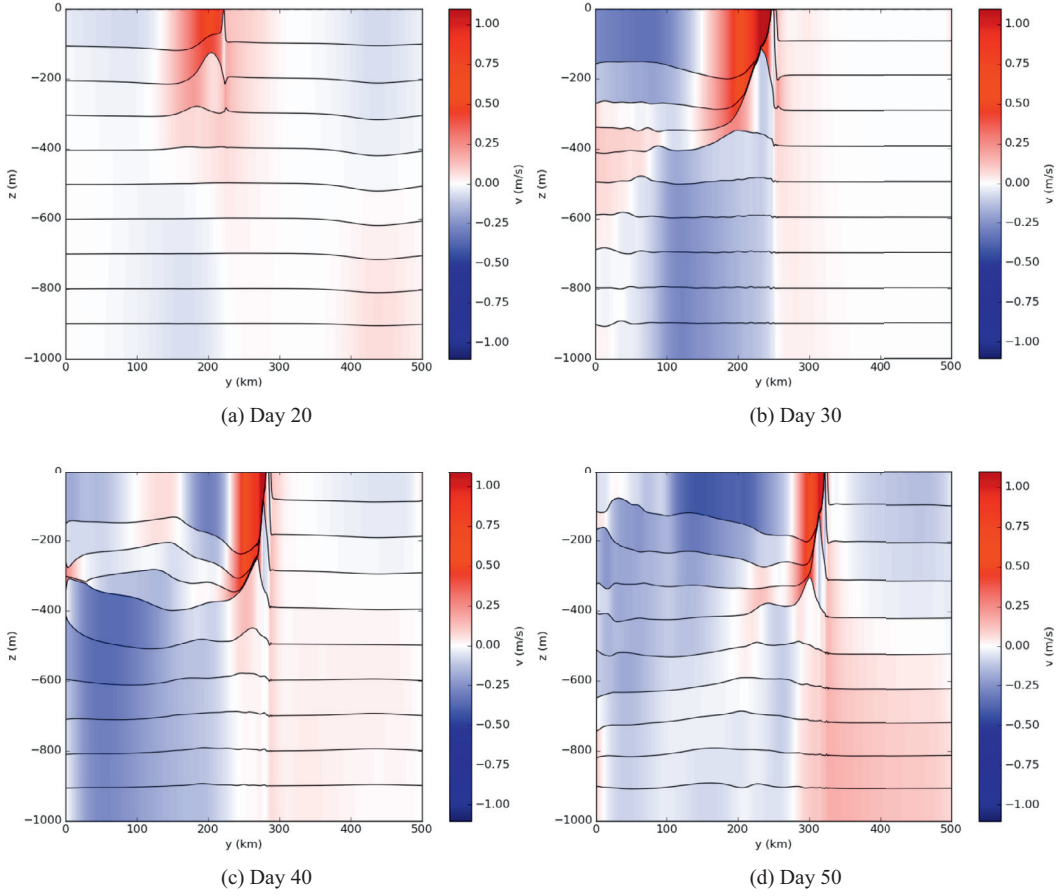


Fig. 8. Snapshots of the along wall velocity (color) and interface displacement (contours) days 20, 30, 40 and 50 for the Q-GCM coupled to the wall equation.

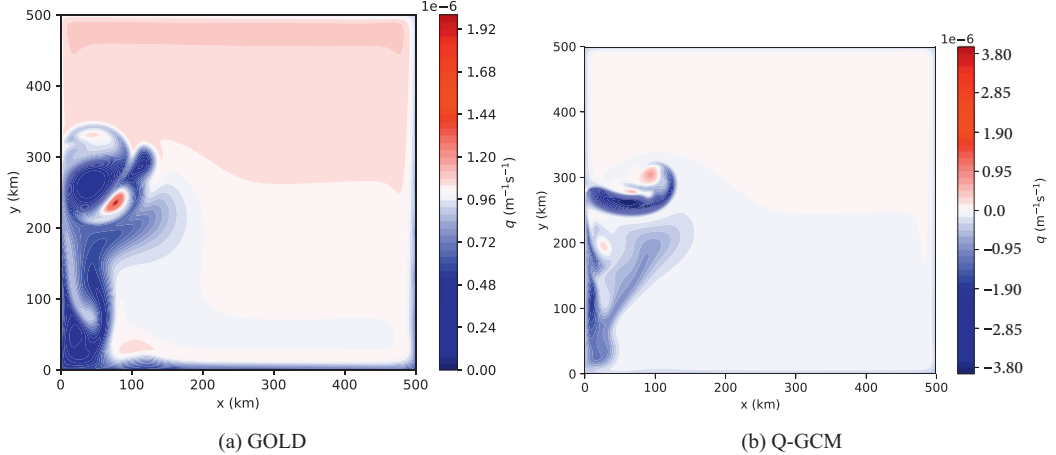


Fig. 9. Potential vorticity fields at Day 40 from GOLD and Q-GCM. Regions of positive potential vorticity coincide with regions of cyclonic vorticity; other regions of cyclonic vorticity are invisible in pv. This is consistent with our theory.

vorticity generation, and thus energy decay, for the duration of the experiments is much less.

5. Summary

We have revisited the problem of boundary conditions for general circulation models. When applied to the problem of a westward drifting vortex encountering a boundary, classical qg implementations with free-slip boundary conditions leave the net circulation of the domain virtually unchanged. In contrast, primitive equation models inject strong cyclonic vorticity into

the domain and as a result lose energy considerably faster when compared to the qg result. We have proposed a boundary layer analysis that, when used in a qg model (effectively as a DBM), endows it with energy and vorticity behavior like that computed from the primitive equation models.

The essence of the analysis is in the interaction between interior balanced dynamics and boundary dynamics, the latter generally arising because of the no-normal flow boundary condition. The wall dynamics are constrained to have no potential vorticity anomaly; for the case of a wall, Kelvin waves are the result. When the interior flow imposes a velocity on the wall in excess of a

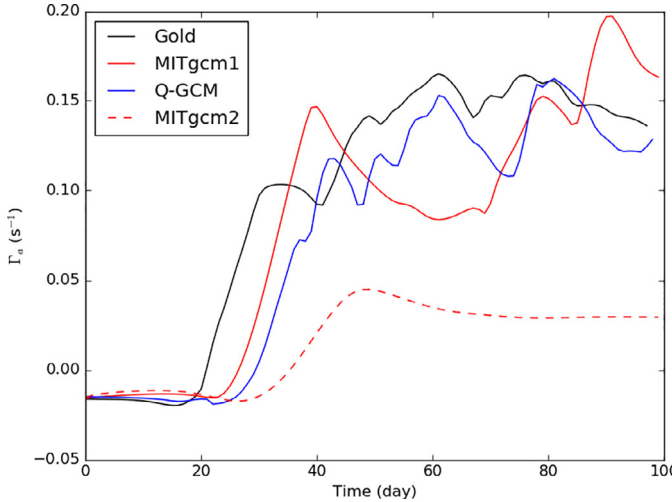


Fig. 10. Time series of the relative vorticity in the upper layer in the 3 configurations. We also added the curve for MITgcm with $v = 50 \text{ m}^2 \text{ s}^{-1}$.

Kelvin wave phase speed, the blocked downstream wave propagation builds a finite amplitude response in the form of fronts. Regularization of the fronts, given their form, requires either viscous or diabatic effects that, when expressed in a pv framework constitute a pv flux from the wall. The size of the flux can be computed from the front characteristics themselves and as such does not require an explicit viscous or diabatic coefficient. The effect of the wall parameterization is to add the frontal pv flux to the preexisting interior pv distribution. This effect, when introduced into qg, qualitatively and quantitatively (if not exactly) amends the qg evolution to that seen in primitive equation models. We have also found that these mechanics effectively drain energy from the interior balanced flow, suggesting that a resolution to the open question of the fate of balanced energy involves boundary dynamics.

While we think of this as a DBM for subgrid-scale parameterization, it describes only a subset of possible interior-boundary interactions. These mechanics require an interior flow counter to the direction of topographic waves; the case of oppositely directed flows remains unstudied. Further, aspects of the present interaction remain unclear. The boundary fronts govern the amplitude of the effect on the interior, but the nature of the frontal dynamics remains unclear. The fronts themselves are related to the pv fluxes, thus making the feedback relatively insensitive to poorly known parameters like eddy diffusivities, but we have also found too large of an eddy viscosity can damp these mechanics. We speculate that the fronts exist in a regime independent of viscous coefficients,

but have yet to uncover this regime. We have also shown only how to amend sub-grid scale qg dynamics with our DBM. Further studies will explore recipes for including these effects into the sub-grid scale parameterization of primitive equations.

Acknowledgments

This work was initiated during a visit by WKD to UCL, partial support for which came from the Sea and Currents Fund of the UCL Global Engagement Office for which the authors are grateful. WKD and BD are also supported under NSF grants 1434780 and 1537304.

Appendix A. An Augmented Jacobian for Stratified QG

The Arakawa Jacobian is routinely used for the advection operator in quasi-geostrophy. While it is generally apt, stratified qg boundary conditions are not necessarily consistent with the classical implementation. The analytical properties of the Jacobian for constant boundary p are

$$\begin{aligned} \int_A J(p, q) dA &= 0 \\ \int_A p J(p, q) dA &= \int_A J\left(\frac{p^2}{2}, q\right) dA = 0 \\ \int_A q J(p, q) dA &= \int_A J\left(p, \frac{q^2}{2}\right) dA = 0 \end{aligned} \quad (\text{A1})$$

because of no normal flow. As shown by [Salmon and Talley \(1989\)](#), the classical Arakawa discretization is consistent with these properties only if the boundary $p(\partial A)$ vanishes, which in a stratified system is not generally true. Equivalently, the classical Arakawa formulation does not meet [\(A1\)](#), as can be shown by straightforward numerical integration. [Holland \(1978\)](#) noticed this and instead developed an energy equation by multiplying the pv equation by a pressure adjusted for the boundary pressure. Here, closely following [Salmon and Talley \(1989\)](#), a generalization to the Arakawa Jacobian is developed that allows for non-zero boundary pressure.

Potential vorticity conservation implies

$$\int_A \alpha \left(\frac{\partial}{\partial t} q + J(p, q) \right) dA = 0 \quad (\text{A2})$$

for any $\alpha(x, y)$. Manipulating the arguments, one can show

$$\int_A \alpha J(p, q) dA = \int_A q J(\alpha, p) dA \quad (\text{A3})$$

by using only the no-normal flow condition on p . However, if the other permutation of arguments is attempted, there results

$$\int_A \alpha J(p, q) dA = \int_A p J(q, \alpha) dA - p(\partial A) \int_{\partial A} \nabla q \cdot \mathbf{t} dl \quad (\text{A4})$$

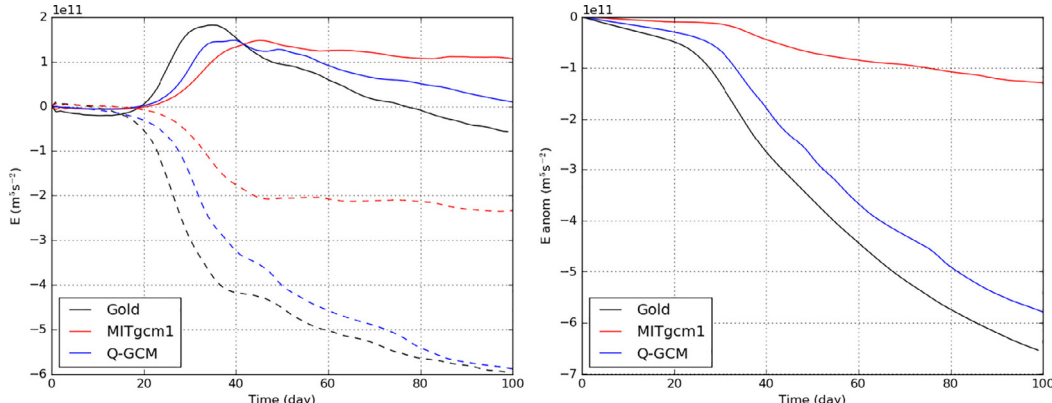


Fig. 11. (left) Time series of the kinetic (solid) and potential (dashed) energy anomalies in the three models. (right) Time series of the total energy from the three model runs.

where \mathbf{t} is the unit vector tangential to the domain boundary. The last integral on the right hand side is not guaranteed to vanish for non-zero boundary pressure.

The integrated Jacobian can in general be written

$$\int_A \alpha J(p, q) dA = a \int_A \alpha J(p, q) dA + b \left(\int_A p J(q, \alpha) dA - p(\partial A) \int_{\partial A} \alpha \nabla q \cdot \mathbf{t} dl \right) + c \int_A q J(\alpha, p) dA \quad (\text{A5})$$

where $a + b + c = 1$. We now express (A2) symbolically in discrete form

$$\begin{aligned} \Sigma_i \delta A_i \alpha_i \left(\frac{\partial}{\partial t} q \right)_i &= \Sigma \delta A_i [a \alpha_i j_i(p_j, q_k) + b p_i j_i(q_j, \alpha_k) \\ &\quad + c q_i j_i(\alpha_j, p_k)] + \delta l_i p(\partial A) \alpha_i (\nabla q)_i \Delta_{i,ib} \\ &= F(\alpha_i, q_j, p_k; a, b, c) \end{aligned} \quad (\text{A6})$$

where δA_i is the area element associated with point i , δl_i the line element associated with boundary point i and $\Delta_{i,ib}$ is the Kronecker delta function defined by

$$\begin{aligned} \Delta_{i,ib} &= 1; i = ib \\ \Delta_{i,ib} &= 0; \text{otherwise} \end{aligned} \quad (\text{A7})$$

with ib the index of a point on the boundary. The [Salmon and Talley \(1989\)](#) notation has been used, but the form of F is different. From (A6), one can show

$$-\frac{\partial}{\partial t} q_i = \frac{\partial}{\partial \alpha_i} F \quad (\text{A8})$$

which specifies the form of the Jacobian that satisfies (A2).

The only modification to (A6) from that appearing in [Salmon and Talley \(1989\)](#) are terms on the boundary, implying that the classical Arakawa discretization applies to the interior gridpoints. On the boundary, the usual discretization must be augmented by any discretization satisfying

$$\oint \nabla q \cdot \mathbf{n} dl = \oint q \nabla \cdot \mathbf{n} dl = 0 \quad (\text{A9})$$

The second order discretization

$$\left(\frac{\partial}{\partial x} q \right)_i = \frac{q_{i+1} - q_{i-1}}{2 \Delta_l} \quad (\text{A10})$$

meets this criterion provided the q in the second line integral is evaluated at point i . Evaluating F and taking the derivative in (A8) determines the required Jacobian stencil. For a point on a north-south wall, the usual discretization must be modified to

$$J_{ib,j}(p, q) = J_{ib,j}(p, q)_{\text{Arakawa}} + p(\partial A)(q(i_b, j+1) - q(i_b, j-1)) \quad (\text{A11})$$

where ib, j are the zonal and meridional indices of a western boundary point. A straightforward modification of the above applies to points on other boundaries.

References

- Adcroft, A., Marshall, D., 1998. How slippery are piecewise-constant coastlines in numerical ocean models? *Tellus* 50A, 95–108.
- Bryan, F., Hecht, M., Smith, R., 2006. Resolution convergence and sensitivity studies with north atlantic circulation models. part i: the western boundary current system. *Ocean Modell.* 16, 141–159.
- Chassignet, E., Garraffo, Z., 2001. Viscosity parameterization and the Gulf Stream separation. In: Muller, P., Henderson, D. (Eds.), *From Stirring to Mixing in a Stratified Ocean*, Aha Huliko'a Hawaiian Winter Workshop, pp. 37–41.
- Crosby, A., Johnson, E., Morrison, P., 2013. Deformation of vortex patches by boundaries. *Phys. Fluids* 25. doi:[10.1063/1.4790809](https://doi.org/10.1063/1.4790809).
- Dewar, W., Berloff, P., Hogg, A., 2011. Submesoscale generation by boundaries. *J. Mar. Res.* 69, 501–522.
- Dewar, W., Hogg, A., 2010. Topographic inviscid dissipation of balanced flow. *Ocean Modell.* 32, 1–13.
- Dewar, W.K., Hogg, A., 2010. Topographic inviscid dissipation of balanced flow. *Ocean Model.* 32, 1–13. doi:[10.1016/j.ocemod.2009.03.007](https://doi.org/10.1016/j.ocemod.2009.03.007).
- Doswell III, C.A., 1984. A kinematic analysis of frontogenesis associated with a nondivergent vortex. *J. Atmos. Sci.* 41, 1242–1248. doi:[10.1175/1520-0469\(1984\)041\(1242:AKAOFA\)2.0.CO;2](https://doi.org/10.1175/1520-0469(1984)041(1242:AKAOFA)2.0.CO;2).
- Haidvogel, D., McWilliams, J., Gent, P., 1992. Boundary current separation in a quasigeostrophic, eddy-resolving ocean circulation model. *J. Phys. Oceanogr.* 22, 882–902.
- Hallberg, R., 2000. Time integration of diapycnal diffusion and richardson number dependent mixing in isopycnal coordinate ocean models. *Mon. Wea. Rev.* 128, 1402. doi:[10.1175/1520-0493\(2000\)128\(1402:TIODDA\)2.0.CO;2](https://doi.org/10.1175/1520-0493(2000)128(1402:TIODDA)2.0.CO;2).
- Hogg, A.M.C., Dewar, W.K., Killworth, P.D., Blundell, J.R., 2003. A quasi-geostrophic coupled model (Q-GCM). *Mon. Wea. Rev.* 131 (10), 2261–2278. doi:[10.1175/1520-0493\(2003\)131\(2261:AQCMQ\)2.0.CO;2](https://doi.org/10.1175/1520-0493(2003)131(2261:AQCMQ)2.0.CO;2).
- Holland, W., 1978. The role of mesoscale eddies in the general circulation of the ocean – numerical experiments using a wind-driven quasi-geostrophic model. *J. Phys. Oceanogr.* 8, 363–392.
- Madec, G., 2006. NEMO Reference Manual, Ocean Dynamic Component: NEMO-OPA. Institut Pierre Simon Laplace. 27th ed.
- Marshall, J., Hill, C., Perelman, L., Adcroft, A., 1997. Hydrostatic, quasi-hydrostatic and non-hydrostatic ocean modelling. *J. Geophys. Res.* 102, 5733–5753.
- Marshall, J., Jamous, D., Nilsson, J., 2001. Entry, flux and exit of potential vorticity in ocean circulation. *J. Phys. Oceanogr.* 31, 777–789.
- McWilliams, J., 1977. A note on a consistent quasigeostrophic model in a multiply connected domain. *Dyn. Atmos. Oceans* 1, 427–441.
- Munk, W., 1950. On the wind-driven ocean circulation. *J. Meteor.* 7, 79–93.
- Pedlosky, J., 2013. Waves in the Ocean and Atmosphere: Introduction to Wave Dynamics. Springer, New York.
- Salmon, R., Talley, L., 1989. Generalizations of Arakawa's Jacobian. *J. Comput. Phys.* 83, 247–259.
- Schoonover, J., Dewar, W., Wienders, N., Deremble, B., 2017. Local sensitivities of the gulf stream separation. *J. Phys. Oceanogr.* 47, 353–373.
- Stommel, H., 1948. The westward intensification of wind-driven ocean currents. *EOS Trans. Am. Geophys. Union* 29, 202–206.
- Whitham, G., 1974. Linear and nonlinear waves. Pure and Applied Mathematics Monographs and Tracts. Wiley Interscience.